Li *et al.*
Chinese Journal of Mechanical Engineering (2024) 37:49
https://doi.org/10.1186/s10033-024-01037-1

Chinese Journal of Mechanical Engineering

ORIGINAL ARTICLE

Open Access

Multi-Physics Coupled Acoustic-Mechanics Analysis and Synergetic Optimization for a Twin-Fluid Atomization Nozzle

Wenying Li[1,2], Yanying Li[3,4], Yingjie Lu[1], Jinhuan Xu[1], Bo Chen[1,2], Li Zhang[1*] and Yanbiao Li[1*]

Abstract

Fine particulate matter produced during the rapid industrialization over the past decades can cause significant harm to human health. Twin-fluid atomization technology is an effective means of controlling fine particulate matter pollution. In this paper, the influences of the main parameters on the droplet size, effective atomization range and sound pressure level (SPL) of a twin-fluid nozzle (TFN) are investigated, and in order to improve the atomization performance, a multi-objective synergetic optimization algorithm is presented. A multi-physics coupled acoustic-mechanics model based on the discrete phase model (DPM), large eddy simulation (LES) model, and Ffowcs Williams-Hawkings (FW-H) model is established, and the numerical simulation results of the multi-physics coupled acoustic-mechanics method are verified via experimental comparison. Based on the analysis of the multi-physics coupled acoustic-mechanics numerical simulation results, the effects of the water flow on the characteristics of the atomization flow distribution were obtained. A multi-physics coupled acoustic-mechanics numerical simulation result was employed to establish an orthogonal test database, and a multi-objective synergetic optimization algorithm was adopted to optimize the key parameters of the TFN. The optimal parameters are as follows: A gas flow of 0.94 m^3/h, water flow of 0.0237 m^3/h, orifice diameter of the self-excited vibrating cavity (SVC) of 1.19 mm, SVC orifice depth of 0.53 mm, distance between SVC and the outlet of nozzle of 5.11 mm, and a nozzle outlet diameter of 3.15 mm. The droplet particle size in the atomization flow field was significantly reduced, the spray distance improved by 71.56%, and the SPL data at each corresponding measurement point decreased by an average of 38.96%. The conclusions of this study offer a references for future TFN research.

Keywords Twin-fluid nozzle, BP neural network, Multi-objective optimization, Multi-physics coupled, Acoustic-mechanics analysis, Genetic algorithm

1 Introduction

Due to the rapid urbanization and industrialization over the past decades, atmospheric pollution has become increasingly severe [1–4]. The excessive discharge of pollutants from industrial production leads to a large number of fine particles entering the atmospheric environment. Fine particles can reach the alveoli of human lungs and cause various respiratory tract and lung diseases [5, 6], causing serious harm to human health. Therefore, reducing the fine particulate matter emissions from diffusive sources is an important issue that must be addressed.

*Correspondence:
Li Zhang
zhangli@zjut.edu.cn
Yanbiao Li
lybrory@zjut.edu.cn
[1] College of Mechanical Engineering, Zhejiang University of Technology, Hangzhou 310023, China
[2] State Key Laboratory of Fluid Power and Mechatronic Systems, Zhejiang University, Hangzhou 310027, China
[3] School of Materials Science and Engineering, Northwestern Polytechnical University, Xian 710072, China
[4] Guizhou Anda Aviation Forging Co., Ltd., Anshun 561005, China

Springer Open

© The Author(s) 2024. **Open Access** This article is licensed under a Creative Commons Attribution 4.0 International License, which permits use, sharing, adaptation, distribution and reproduction in any medium or format, as long as you give appropriate credit to the original author(s) and the source, provide a link to the Creative Commons licence, and indicate if changes were made. The images or other third party material in this article are included in the article's Creative Commons licence, unless indicated otherwise in a credit line to the material. If material is not included in the article's Creative Commons licence and your intended use is not permitted by statutory regulation or exceeds the permitted use, you will need to obtain permission directly from the copyright holder. To view a copy of this licence, visit http://creativecommons.org/licenses/by/4.0/.

As a key component of wet dust removal equipment, atomizing nozzles use the generated fine mist droplets to capture dust particles and are widely used in the industry [7–9]. However, because of the large areas in industrial application scenarios, droplet coverage needs to cover a huge area, and it is often necessary to install a large number of atomizing nozzles to achieve an effective removal of fine particles. The noise generated by the large number of nozzles, however, has a very negative influence on the working environment [10]. Thus, reducing the droplet size, increasing the effective range of nozzle atomization, and reducing the noise of the atomizing nozzles are pivotal problems to be solved, and many investigations have been conducted on these topics.

Zhou et al. [11] designed a centrifugal atomization test device for small drone pesticide rotor cup nozzles and optimized the structural parameters of the rotor nozzle using variance analysis and a quadratic regression orthogonal test. Li et al. [12] studied the influence of sine waves on mixed hydrogen cross-flow jets using numerical simulations and compared the mixing zones of different modes. Wang et al. [13] experimentally investigated the atomization properties and dust-suppression performance of an X-swirl nozzle. The influence of the diameter of the water outlet and the pressure of the water inlet on the nozzle parameters was comprehensively analyzed, and the nozzle diameter parameters were optimized under the condition of a low water supply pressure. Akkoli et al. [14] developed a CFD model of a diesel engine for numerical simulation, investigated the combined effects of the injector parameters on the emission characteristics of the engine by varying the geometry of the injector nozzle and determined the optimal parameters for reduced emission levels.

The aforementioned research on structural parameter optimization and optimization methods for atomizing nozzles provides an important reference. However, these studies on atomizers mainly focused on a single-fluid medium, and the interactions between two fluid media need to be studied in more detail.

Recently, nozzle characteristics were investigated using the DPM model or Ffowcs Williams-Hawkings (FW-H) model. Li et al. [15] developed an isometric model of a vortex ventilation system and a discrete phase model (DPM) for numerical simulations to investigate the parameter distribution for different flow ratios and obtain a suitable axial-radial flow ratio. Thompson et al. [16] performed three-dimensional axisymmetric simulations of atomized gas nozzle configurations to evaluate the influence of the process parameters on the final particle size of the produced metal powders and used numerical simulations to qualitatively assess the effects of the atomized nozzle geometry and process conditions on the average size of the produced powders. Chen et al. [17] investigated the three-dimensional transient flow, temperature, solidification, segregation, and inclusion transfer during slab continuous casting and successfully predicted the number, size, and spatial distribution of inclusions in the cross sections of the continuous casting slabs. The aforementioned studies have made some progress using the DPM-LES or FW-H model for investigating the flow field peculiarity of the twin-fluid nozzle (TFN). However, none of these studies considered the coupled influence of flow and acoustic fields. However, in a real situation, the acoustic characteristics of the nozzle change significantly because of the intense interactions between the gas and liquid phases and the wall of the TFN. Moreover, acoustic peculiarities influence unstable surface waves [18], thereby affecting the droplet diameter. Consequently, it is more accurate to use the multi-physics coupled acoustic-mechanics model for simulating the working conditions.

TFN has become a popular research topic because of its characteristics of producing a small droplet size and a superior atomization effect. However, TFN is also very noisy and has other disadvantages. Therefore, improving the atomization efficiency and reducing the noise are urgent problems to be solved. Jedelský et al. [19] provided an experimental study of a porous TFN. The experiments showed the spatial distribution of the spray using phase Doppler anemometry and studied the droplet size-velocity correlation and dimensions. Jeong et al. [20] studied the spray characteristics of a TFN considering water mist and its heptane pool fire extinguishing performance. Pezo et al. [21] investigated the influence of different nozzle diameters and fluid temperatures on the jet characteristics using experimental and computational methods. Zhang et al. [22] added a zigzag structure to a spherical tuyere to reduce the jet noise, which provided a reference for the low-noise optimization of a spherical tuyere.

In summary, studies on the optimization of twin-fluid atomization nozzles have focused on single-component structures and single optimization methods. Few studies have been conducted on the multi-parameter, multi-objective synergetic optimization of the entire structure. However, a multi-parameter and multi-objective analysis of the overall structure of a TFN is key to improving its efficiency. In our previous work, Chen et al. [23, 24] analyzed and compared the effects of self-excited vibrating cavity (SVC) on the spray performance of TFN using the phase Doppler method. Numerical analysis and comparative experiments on twin-fluid atomization nozzles under different parameter conditions were conducted, and the effects of different gas-liquid pressure

ratios and structural parameters on the atomization performance were studied in detail. The results indicate that the SVC structure promotes the secondary atomization performance of a TFN and the study provides a reference for the optimized design of TFN.

In this study, a TFN was selected, and a method combining a multi-physics coupled acoustic-mechanics numerical simulation and an intelligent synergetic optimization algorithm was adopted for optimizing the key parts of the overall structure of the TFN. By analyzing the numerical simulation results of the multi-physics coupled acoustic mechanics, the effects of the water flow rate on the characteristics of the atomization flow field were obtained. Furthermore, the comprehensive effects of the main parameters of TFN on the droplet size, effective atomization range and sound pressure level (SPL) were investigated in detail, a multi-objective synergetic optimization scheme was determined, and validation tests were carried out to verify the validity of the optimization model with a physical prototype.

2 Methodology

2.1 Mathematic Model

2.1.1 Mathematic Model of Nozzle Flow Field

During the atomization process of the TFN in this study, compressed air intensified the instability of the liquid phase membrane interior and exterior of the nozzle and accelerated the fragmentation of the liquid phase membrane into tiny particle-size droplets, which enhanced the atomization performance of the TFN. Turbulence, cavitation, aerodynamic disturbances, and droplet fragmentation can be considered synthetically using the Euler-Lagrange method. The DPM model based on the Euler-Lagrange method meets the requirements for the simulation of a TFN [25]. In the DPM, the trajectory of the droplets can be solved by computing the differential equations of the forces acting on the particles in the Lagrange coordinate system. The differential equation describing the trajectory of the liquid droplets is represented in the Cartesian coordinate system, as follows:

$$\begin{aligned}\frac{\mathrm{d}u_{p,\,x}}{\mathrm{d}t} &= F_D(u_{l,\,x}-u_{p,\,x})+\frac{g_x(\rho_p-\rho_l)}{\rho_p}-D_{T,p}\frac{1}{m_pT}\frac{\partial T}{\partial x},\\ \frac{\mathrm{d}u_{p,\,y}}{\mathrm{d}t} &= F_D(u_{l,\,y}-u_{p,\,y})+\frac{g_y(\rho_p-\rho_l)}{\rho_p}-D_{T,p}\frac{1}{m_pT}\frac{\partial T}{\partial y},\\ \frac{\mathrm{d}u_{p,\,z}}{\mathrm{d}t} &= F_D(u_{l,\,z}-u_{p,\,z})+\frac{g_z(\rho_p-\rho_l)}{\rho_p}-D_{T,p}\frac{1}{m_pT}\frac{\partial T}{\partial z}.\end{aligned} \tag{1}$$

where u_p is the velocity of the discrete phase particles, F_D is the drag force on the discrete phase particles, u_l is the velocity of the continuous phase fluid, ρ_p is the density of the discrete phase particles, ρ_l is the density of the continuous phase fluid, m_p is the mass of the discrete phase particles, T is the fluid temperature, $D_{T,p}$ is the thermal swimming force coefficient, and t is the time.

The narrow flow space inside the TFN, extremely high fluid-phase flow velocity, high atomization time, and strong turbulence can easily lead to the generation of a local vortex. To precisely simulate the TFN atomization process, the large eddy simulation (LES) model was used to conduct a numerical simulation [26]. The LES control equation is expressed as:

$$\begin{aligned}&\frac{\partial\rho}{\partial t}+\frac{\partial\rho\overline{u_i}}{\partial t}=0,\\ &\frac{\partial}{\partial t}(\rho\overline{u_i})+\frac{\partial}{\partial x_j}\left(\rho\overline{u_iu_j}\right)=\frac{\partial}{\partial x_j}\left(\mu\frac{\partial\overline{u_i}}{\partial x_j}\right)-\frac{\partial\overline{p}}{\partial x_j}-\frac{\partial\tau_{ij}}{\partial x_i},\end{aligned} \tag{2}$$

where τ_{ij} is the sub-mesh stress, $\tau_{ij}=\rho\overline{u_iu_j}-\rho\overline{u_i}\cdot\overline{u_j}$, x_i and x_j are the coordinate components, the i and j indices are (1, 2, 3), $\bar{u}_i$ and $\bar{u}_j$ is the instantaneous filtering speed, p is the pressure on the fluid unit, ρ is fluid density, and μ is the dynamic viscosity.

2.1.2 Mathematic Model of Nozzle Acoustic Field

Many droplets were ejected and impacted the oscillation cavity, causing it to vibrate at a higher frequency during atomization. High-frequency oscillations in the oscillation cavity can generate sound waves. Their size reflects the strength and energy of the sound waves. Any change in the sound wave has an important influence on the fragmentation of the droplets, which is another important factor affecting the atomization performance of the TFN. Therefore, it is necessary to study the acoustic characteristics of the TFN, which is conducive to further understanding the atomization properties of the TFN in multi-physics coupling.

The additional pressure caused by the vibrations of sound waves is called sound pressure. The consequence of sound pressure is a change in the atmospheric pressure caused by the vibrations of the sound waves. Sound pressure is an important indicator of the sound field characteristics and an important characteristic of the sound wave intensity. Sound pressure level (SPL) is often used to define sound pressure.

The instantaneous sound pressure value at a certain moment in the sound field generated by the sound source is expressed as:

$$p(x,t)=p_m\cos(\omega_1t-k_wx), \tag{3}$$

where p_m is the amplitude of the sound pressure, ω_1 is the angular frequency of the vibration, k_w is the wave number, and $k_w x$ is the initial phase.

The effective sound pressure can be obtained by taking the instantaneous sound pressure from a specific time interval and calculating the root mean square of the time. The formula is as follows:

$$p_a = \sqrt{\frac{1}{t}\int_0^t p^2(x,t)\mathrm{d}t}. \tag{4}$$

The variable form of the effective sound pressure could be acquired by substituting Eq. (3) into Eq. (4):

$$p_a = \frac{p_m}{\sqrt{2}}. \tag{5}$$

In Eq. (5), the effective sound pressure p_a can be calculated if the sound pressure amplitude p_m is obtained. The relationship between L_P and the effective sound pressure p_a is as follows:

$$L_P = 20\log\frac{p_a}{p_0}, \tag{6}$$

where p_0 is the reference sound pressure value, usually p_0 is 2×10^{-5} Pa.

2.1.3 Multi-Physics Coupled Acoustic-Mechanics Model

In this study, the flow of the gas-liquid two-phase and the droplets in the flow field was extremely complex during the atomization of the TFN. The vibrations of the SVC significantly influenced the turbulence of the flow field and caused noise. Therefore, this problem involves multi-physics coupling. It is necessary to integrate knowledge on bidirectional fluid-solid coupling, computational aeroacoustics, and discrete phase models to build a multi-physics coupled acoustic-mechanical model for the multi-physics coupling numerical simulation of the TFN.

The hybrid method in the computational aero-acoustics (CAA) simplifies the entire acoustic field calculation area by making a reasonable distinction between the source area, where the fluid itself generates the acoustic field, and the propagation area, where the sound source diffuses. Moreover, the nonlinear effect distinguished between the fluid and solid phases, which significantly reduced the computational effort of the numerical simulation.

In the TFN, the interactions of the internal fluid with the solid boundary cause acoustic problems; therefore, the FW-H model is adopted, which can be described as follows [27]:

$$\left[\frac{1}{c_0^2}\frac{\partial}{\partial t^2} - \nabla^2\right]\left[c_0^2(\rho-\rho_0)H(f)\right] = \frac{\partial}{\partial t}\left(\rho_0 u_i\frac{\partial H}{\partial x_i}\right) - \frac{\partial}{\partial x_i}\left[\sigma_{ij}(p-p_0)\delta(f)\frac{\partial H}{\partial x_i}\right] + \frac{\partial^2\left(T_{ij}H(f)\right)}{\partial x_i\partial x_j}. \tag{7}$$

The right-hand side of the equation represents the monopole, dipole, and quadrupole source terms. c_0 is the far-field velocity of the sound, ρ_0 is the undisturbed density, p_0 is the undisturbed pressure, $H(f)$ is the Heaviside function, σ_{ij} is the Kronecker symbol, $\delta(f)$ is the Dirac function, P_{ij} is the stress tensor, and T_{ij} is the Lighthill tensor.

2.2 Numerical Simulation

2.2.1 Physics Model and Operating Conditions

The operating conditions and structure parameters of the TFN were as shown in Table 1.A 3D model is shown in Figure 1.

The turbulent flow in a TFN is extremely complicated, and to simulate the atomization progress more precisely, it is necessary to establish a large flow field area external to the TFN. Therefore, a square area of 1.5 × 1.5 × 4.0 m is set up as the external flow field. Figure 2(a) shows the CFD mesh interior of the TFN and a CFD mesh model is shown in Figure 2(b).

The internal region of the TFN presents a complex gas-liquid coupled problem owing to its small structure size, high local pressure, and intense turbulence. The CFD model of the TFN atomization was meshed using the grid partitioning strategy. The situation is particularly complicated at the confluence of the gas and liquid phases, as well as in the region between the TFN outlet and SVC. Therefore, this region must be meshed using nonstructural tetrahedral grids. Owing to the large region and regular space of the exterior flow field of the TFN, a regular hexahedral grid can be adopted to reduce the number of grids, reduce the calculation time, and save computer resources. The entire mesh model of the TFN flow field consists of a mixed mesh with 2534893 mesh cells and 2297503 mesh nodes. There were 195866 mesh cells inside the nozzle with an average cell size of 1.2 mm. Meanwhile, 2339027 mesh cells were set in the exterior region, with an average cell size of 30 mm.

2.2.2 Multi-Physics Coupled Acoustic-Mechanics Numerical Simulation Method

In this study, the ANSYS Workbench platform was used for performing numerical simulations. First, the flow field and structural models were set up in advance, and the wall surface was defined as a

Table 1 Operating conditions and structure parameters of TFN

Parameter	Initial value
Gas flow Q_1 (m^3/h)	1.0
Water flow Q_2 (m^3/h)	0.035
Compressed air inlet diameter *J* (mm)	4.5
Water inlet diameter *R* (mm)	0.8
Distance *S* (mm)	3.0
SVC length *P* (mm)	7.8
SVC diameter *N* (mm)	3.4
Nozzle outlet diameter *H* (mm)	2.3
Orifice depth *L* (mm)	1.5
Orifice diameter *D* (mm)	2.0
Compression section *K* (mm)	4.73
Throat section *M* (mm)	1.06
Expansion section *T* (mm)	3.71

fluid-solid coupled surface in the SVC. Second, the fluid-solid coupled surface was set in Fluent, and the transient structure was mated by the System Coupling solver to accurately establish the bidirectional fluid-solid coupling model. Third, the data from the coupling surfaces were iterated and exchanged in the coupling solver to obtain the variation patterns of the flow and structural fields of the TFN.

Finally, based on bidirectional fluid-solid coupling, a multi-field coupling analysis was performed by adding the acoustic phase and spray phase modules through Fluent. The FW-H model, LES, and DPM models were matched with each other to construct a multi-physics coupled acoustic-mechanics model for integrally investigating any changes in the physical phases, such as the pressure, velocity, and acoustic phases in the flow field. The DPM parameters are listed in Table 2.

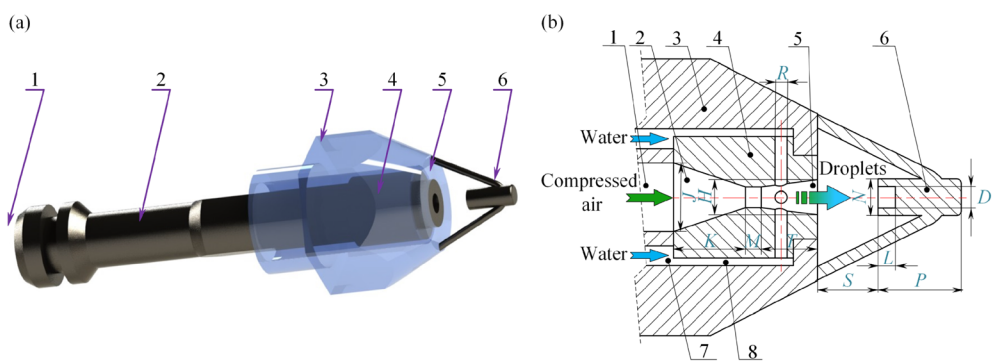

1-air inlet, 2-air channel, 3-nozzle shell, 4-atomizing core, 5-nozzle outlet, 6-self-excited vibrating cavity, 7-water inlet, 8-water channel

Figure 1 TFN model: (**a**) 3D physical model, (**b**) Cutaway view of TFN

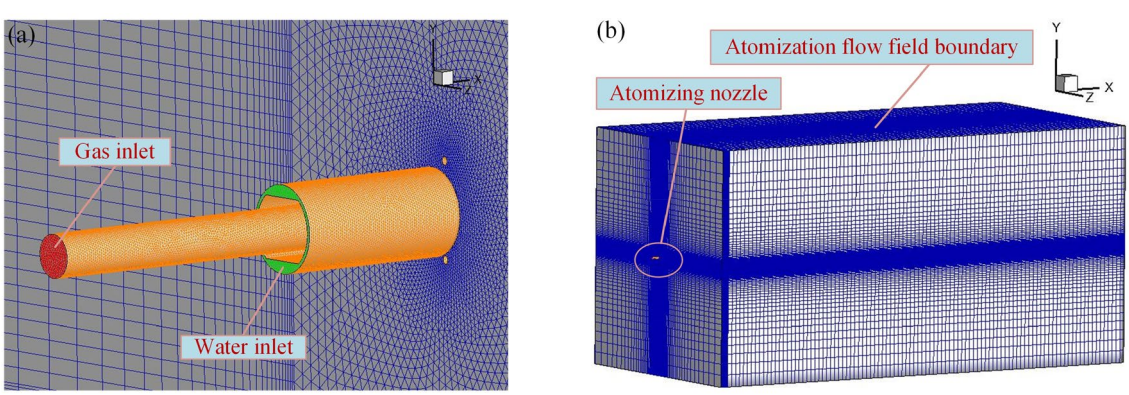

Figure 2 Mesh model: (**a**) Interior mesh model of TFN, (**b**) External mesh model of TFN

Table 2 DPM model parameters

Parameter	Value
Particle tracking time step Δt (s)	1×10^{-4}
Particle velocity (m/s)	10
Particle density (kg/m^3)	1000
Particle diameter (m)	1.2×10^{-3}
Particle angular velocity (rad/s)	5
Particle shape	Customized
Particle injection type	Surface
Number of injected particles	1×10^{4}
Temperature (℃)	25
Thermal conductivity (W/(m·K))	0.59

Table 3 Physics parameters and initial values

Physics parameters	Initial value
Air density (kg/m^3)	1.184
Water density (kg/m^3)	997.1
Air viscosity (mPa·s)	0.01834
Water viscosity (mPa·s)	0.8937
Droplet surface tension (N/m)	0.072
Droplet initial mass flow (kg/s)	0.01
Earth's gravity (m/s^2)	9.81

2.2.3 Boundary Conditions

Using the multi-physics coupled acoustic-mechanics model, a numerical simulation was used for researching the atomization process. The physical parameters of water and air were set in the solver, and water and air were set as the main media for the TFN. Table 3 shows the main physics parameters and initial values (25 ℃ and 101.325 kPa). The finite volume method was adopted and the SIMPLE arithmetic was used.

2.2.4 Grid Independence Verification

From an analysis of the grid-independence verification shown in Table 4, it was determined that a change in the number of grids inside the TFN had a greater influence on the calculation results than the number of grids outside the TFN within a certain boundary. This is because the interior structure of the TFN is extremely complex, and the use of an unstructured mesh, the mesh quality, and density of the calculation results have a more important effect. Simultaneously, the regional structure of the TFN outflow field was well organized, and the number of grids had a small impact on the calculation results. According to the analysis, with an increase in the mesh number, the deviation in the mesh numbers inside and outside the TFN could be controlled to within 0.5%, and the deviation was very small. Therefore, we believe that grid-independent validation (2 million grid count levels) has been completed, and that any subsequent computational analysis based on this grid number is reasonable and reliable.

Table 4 Verification results of mesh independence

Grid area	Grid number	Average droplet size (μm)	Deviation (%)
Inside the nozzle	41587	40.74	4.769
	83692	42.61	0.397
	195545	42.78	0
	316259	42.67	0.257
	402463	42.71	0.164
Outside the nozzle	1205417	41.24	3.600
	1953826	42.85	0.164
	2340242	42.78	0
	3057419	42.73	0.117
	4854761	42.68	0.234

2.2.5 Acoustic Field Model

A multi-physics coupled acoustic field characteristic model of a TFN was established, and the SPL was used as the main assessment criterion for revealing the effects of the process parameters and parameters of the atomizing nozzle on the SPL of the TFN. Before starting a numerical simulation in a multi-physics coupled acoustic field, it is necessary to collect SPL data by setting up multiple spatial monitoring points. Therefore, by considering the center of the TFN outlet as the coordinate origin, five monitoring points were set in the radial and axial directions of the TFN. Figure 3 shows a coordinate chart of the SPL monitoring points and Table 5 lists the coordinate information.

2.3 Twin-Fluid Atomization Experiments

In this study, an atomization test system was designed to conduct spray tests on a TFN. Figure 4 illustrates the design principles and components. It consists of two

Table 5 Coordinate information

Axial monitoring point	Coordinate (mm)	Radial monitoring point	Coordinate (mm)
1	(0, 0, 0)	6	(200, 0, 50)
2	(100, 0, 0)	7	(200, 0, 100)
3	(200, 0, 0)	8	(200, 0, 150)
4	(300, 0, 0)	9	(200, 0, 200)
5	(400, 0, 0)	10	(200, 0, 250)

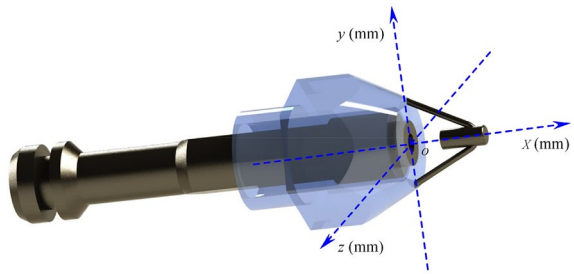

Figure 3 Coordinate chart of SPL monitoring points of TFN

parts: a two-fluid atomization system and a phase Doppler particle analyzer (PDPA, Dantec). The twin-fluid atomization system was used to control and monitor the operating parameters of the test process. Air and water were used as working liquids. The atmospheric pressure was 102.6 kPa and the ambient temperature was 24 ℃ [28].

A PDPA system was used to measure the size distribution, diameter, droplet concentration, and axial velocity. Figure 5 shows a physical diagram of the device. Each test was repeated three times to ensure the accuracy and reliability of the results. The overall uncertainty in the droplet velocity and size was approximately 5% considering random error, statistical uncertainty, and systematic error. Specific parameters and experimental details can be found in another article published by our team, see Ref. [29].

The acoustic field test is mainly measured by the SPL that measured by the sound level meter. The test instrument used is the Sigma brand handheld high-precision AR854 sound level meter, the frequency response is 20–8000 Hz, its measurement range is 30–130 dB, and the measurement accuracy is ± 1.5 dB. As the atomized flow field of the TFN interfered with the test instrument to a certain extent, the test was conducted by selecting multiple measurement points mainly in the radial direction of the TFN. To exclude the impact of any background noise, the measurement time was chosen to be late at night, and the impact of any ambient noise on the measurement value was minimized. To accurately locate the position of the measured space point, we used a tape measure to measure the distance between each measurement point before the measurement and then carried out data collection.

2.4 Verification and Analysis of Numerical Simulation

To verify the numerical simulation, spray process data of the atomization flow field, SMD distribution of the droplets on the nozzle center axis, and SPL were extracted and compared with the test results.

Multi-physics-coupled numerical simulations of the TFN were performed under operating conditions. The particle size distributions at different positions were obtained. The gas flow Q_1 was 1.0 m^3/h and the water flow Q_2 was 0.025–0.04 m^3/h.

As shown in Figure 6, the variation law of the SMD presented by the simulation was consistent with the

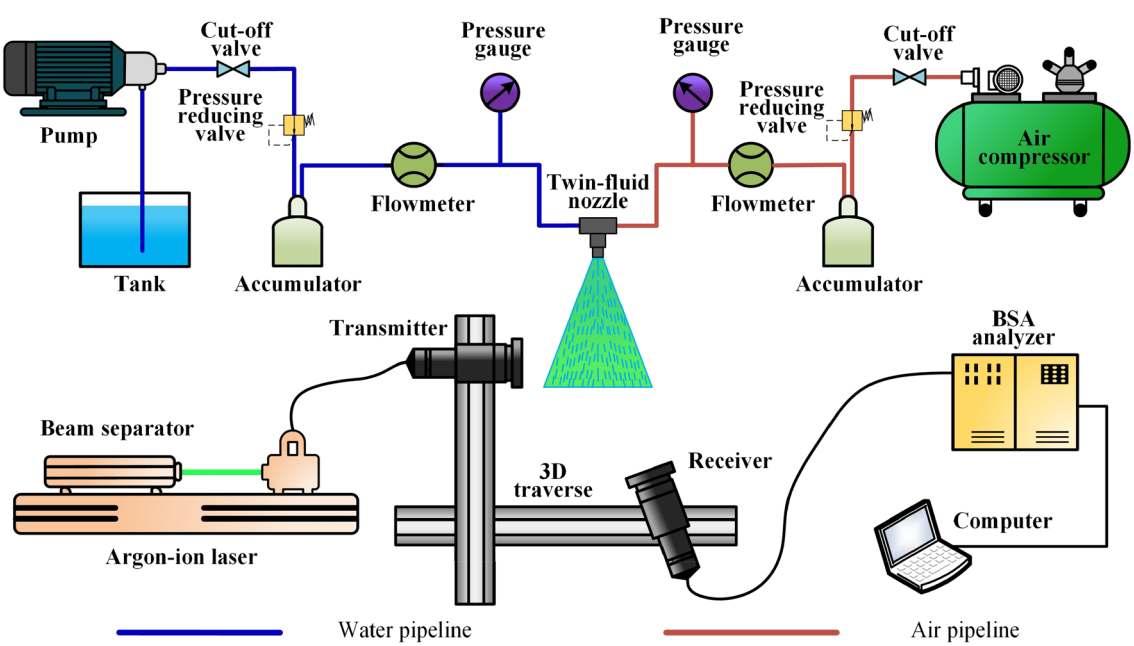

Figure 4 Flow diagram of experimental setup for twin-fluid atomization

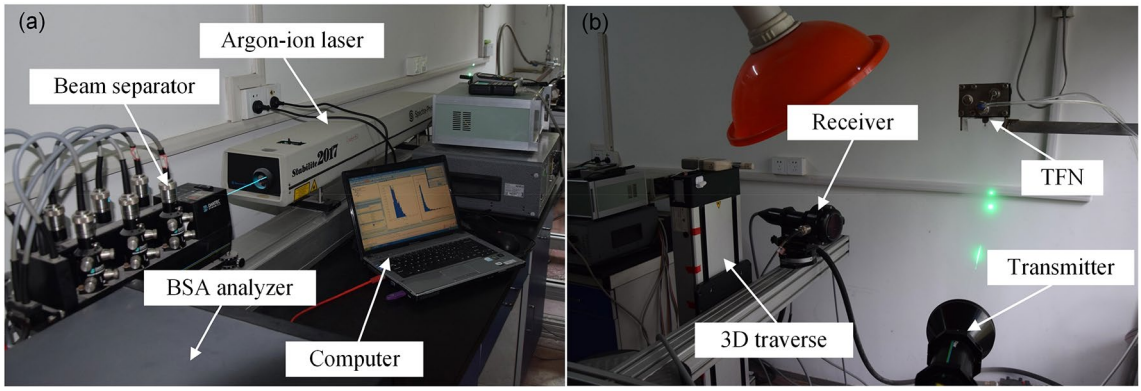

Figure 5 Actual device view of the PDPA system: (**a**) Main component, (**b**) Measuring probe

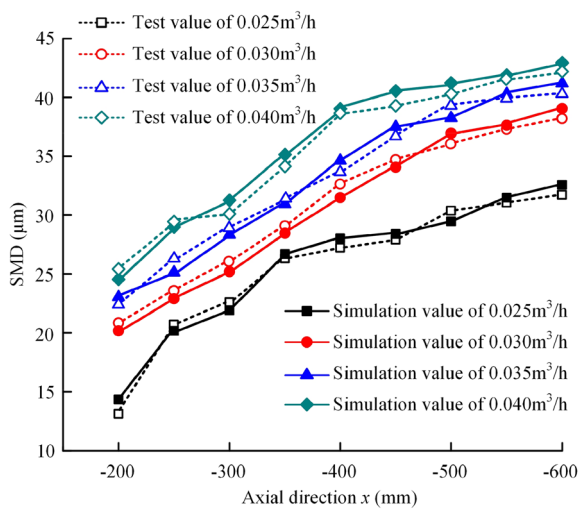

Figure 6 Comparison of simulations and experiments for droplet SMD

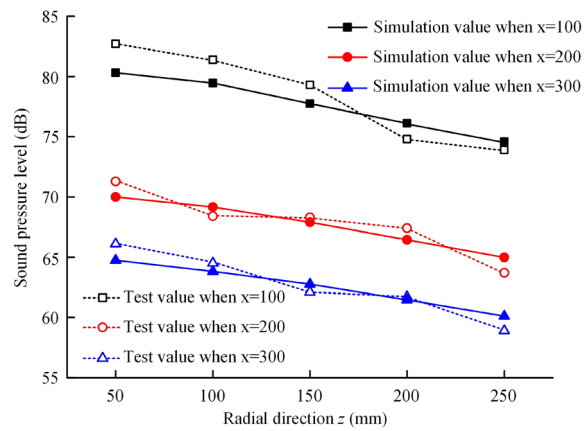

Figure 7 Comparison of simulations and experiments for SPL

experimental test, and the SMD variation pattern was similar to the curve presented in the test results. The error was small, with a maximum error of 5.42%. Based on this analysis, the multi-physics coupled acoustic-mechanics numerical simulation significantly improved the precision in predicting the atomization flow field characteristics, indicating that the multi-physics coupled acoustic-mechanics model has a high accuracy.

The above-mentioned nozzle structure is used for multi-physics coupled acoustic-mechanics numerical simulation calculations and experimental tests with Q_1=1.0 m^3/h and Q_2=0.03 m^3/h. Meanwhile, five measuring points were selected along the radial direction at the axial positions of the nozzle of 100, 200, and 300 mm, and the spacing between the measuring points was 50 mm. Subsequently, the simulation data of the SPL were extracted from the numerical simulation and compared with the test results.

As shown in Figure 7, the pattern of the nozzle SPL distribution along the radial direction simulated by the numerical simulation is in accordance with the experimental results, and the variation pattern of the SPL for different axial distances is in close agreement with the experimental results.

In summary, the results of the multi-physics coupled acoustic-mechanics analysis were consistent with the test results. This indicates that the multi-physics coupled acoustic-mechanics model is precise and that the simulation is reasonable.

3 Multi-Physics Coupled Acoustic-Mechanics Analysis

To analyze the influence of various working parameters on the atomization flow field, the flow field distribution of the TFN was obtained using a multi-physics coupled acoustic-mechanics model. Previous studies have shown that the spray velocity has an important influence on both the particle size and distance,

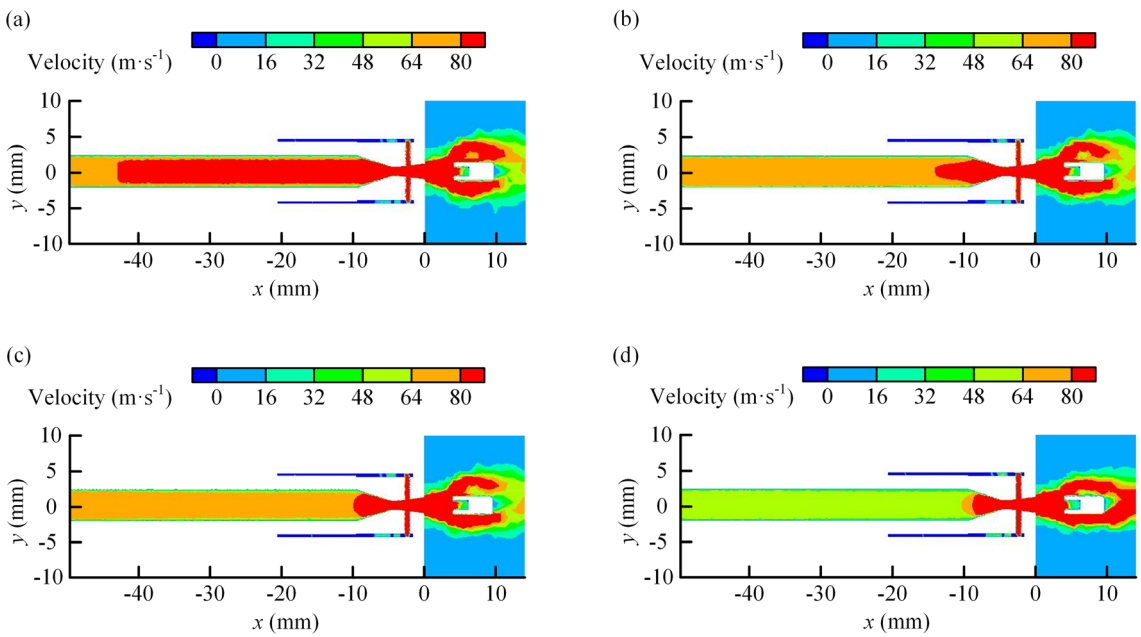

Figure 8 Effect of the water flow on the velocity distribution of the flow field inside TFN: (**a**) Q_2=0.025 m^3/h, (**b**) Q_2=0.03 m^3/h, (**c**) Q_2=0.035 m^3/h, (**d**) Q_2=0.04 m^3/h

with a higher spray velocity favoring droplet breakup, resulting in a smaller overall droplet size and a longer spray distance [23]. Therefore, the water flow rate was selected as the variable for analyzing the effect of the water flow rate variation on the overall atomization flow field characteristics, and the effect of the water flow rate variation on the spray velocity was investigated.

3.1 Effect of Water Flow on Spray Velocity

3.1.1 Effect of Water Flow on Velocity Distribution

Figure 8 shows the distribution law of the internal velocity field of TFN for various water flow rates, and it is obvious by comparison that as the water flow rate increases, the internal velocity of TFN shows a decreasing trend. This is because an increase in the water flow led to an increase in the internal flow resistance of the TFN. The most intuitive manifestation of the increase in the internal flow resistance of the TFN was the reduction in velocity, which resulted in a decrease in the internal velocity of the TFN as the water flow increased.

Moreover, when the water flow rate was Q_2 = 0.035 m^3/h, the velocity of most areas inside the nozzle exceeded 80 m/s. When Q_2 was further increased, the flow velocity inside the TFN decreased to a certain extent, resulting in a smaller difference between the gas and liquid flow velocities.

3.1.2 Effect of Water Flow on Velocity Vector

Based on the simulation results of the multi-physics coupled acoustic-mechanics model, the internal velocity vector diagram of the TFN under various Q_2 values was drawn, as shown in Figure 9.

As shown in Figure 9(a)–(d), although the velocity vector inside the TFN changes significantly with an increase in the water flow rate, it has little influence on the velocity vector at the outlet region of the TFN. As the velocity at the outlet was not significantly affected by the water flow, there was no obvious change in the velocity trajectory or eddy current phenomenon in this area. Although the flow-field disturbance in the SVC region was relatively severe, the velocity vectors in the surrounding regions were not significantly disturbed. Compared with the influence of the gas flow rate, a change in the water flow rate had a weak influence on the velocity vector at the outlet of the TFN and around the SVC.

3.2 Influence of Water Flow Variation on SPL

3.2.1 Changes of SPL in Axial Direction of TFN

The variation rule of the axial distribution of the SPL for different water flows Q_2 is shown in Figure 10. By comparing the changes in the axial distribution of the SPL, it was found that the SPL of the TFN decreased with an increase in the axial distance. At the nozzle outlet with an axial distance of 100 mm, the SPL decreased significantly by approximately 47.6%. As the axial distance increased, the SPL slowly decreased. When the axial distance

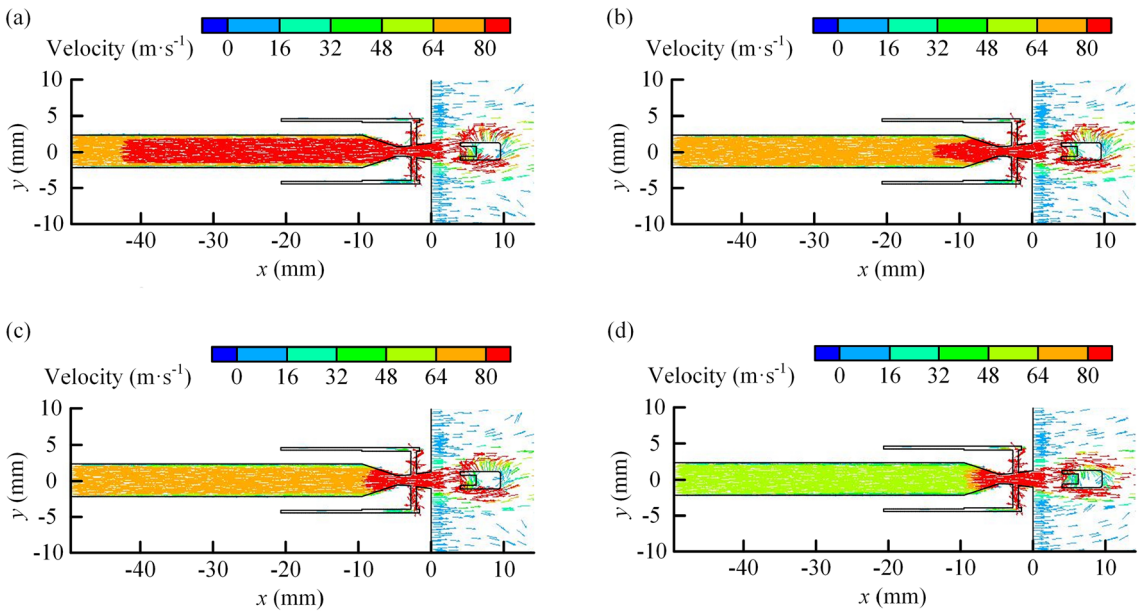

Figure 9 Effect of water flow on the velocity vector of flow field inside TFN: (**a**) Q_2=0.025 m^3/h, (**b**) Q_2=0.03 m^3/h, (**c**) Q_2=0.035 m^3/h, (**d**) Q_2=0.04 m^3/h

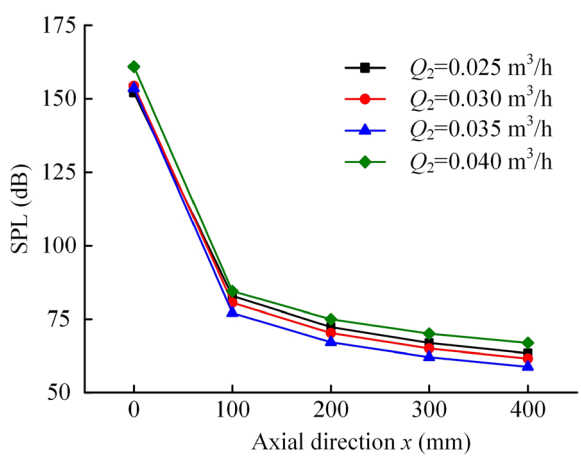

Figure 10 Effect of water flow on axial distribution of SPL

increased from 100 to 400 mm, the SPL decreased by 12.5%, 7.3%, and 5.1%, respectively. The decay rate of the SPL gradually decreased beyond an axial distance of 100 mm, and this phenomenon is mainly related to the energy loss during the axial propagation of acoustic waves.

In addition, comparing the law of change of SPL under various water flows, it was found that with an increase in the water flow, the nozzle axial direction of SPL showed a tendency to first decrease and then increase, but the overall change in SPL between different water flows was not large. At 400 mm from the outlet of the TFN, the SPL varied between 57 and 67 dB for four different water flow rates, and the noise was significantly reduced compared with the high decibel noise at the nozzle outlet.

3.2.2 Changes of SPL in Radial Direction of TFN

Figure 11 shows the variation in the radial distribution of the SPL under different water flow rates at an axial distance of 200 mm. By comparison with the change law of the radial distribution of the SPL, it was found that the SPL of the nozzle gradually decreased with increasing radial distance. For the radial distance studied, the overall decrease in the SPL of the TFN at different water flow rates was approximately 7.9%. This is because the measurement points are distributed outside the strong turbulence zone, and the influence of the turbulence weakens the decrease in the SPL. From the point of view of the nozzle operating noise, Q_2 = 0.035 m^3/h is considered a good choice for the nozzle operating parameters.

4 Multi-Objective Synergetic Optimization Method

4.1 Determination of Multi-Objective Synergetic Optimization Algorithm Scheme

From the simulation results, it is found that the operational parameters and parameters of the twin-fluid nozzle (TFN) have some effect on each characteristic index. Considering the multifaceted indicators of a TFN in order to improve its comprehensive performance in all

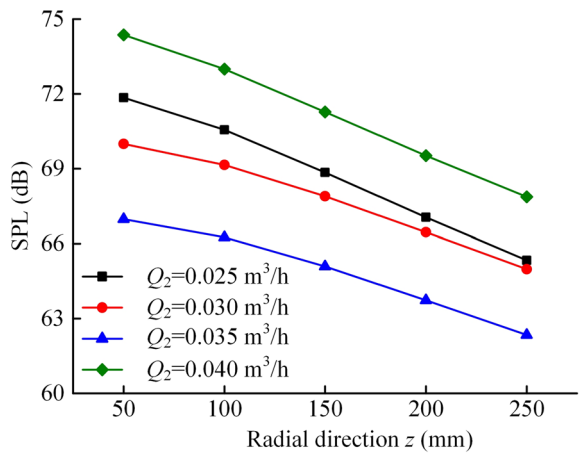

Figure 11 Effect of water flow on radial distribution of SPL

aspects and achieve maximum optimization, it is crucial to conduct a multi-objective synergetic optimization algorithm study of the TFN.

In this study, a multi-objective synergetic optimization algorithm method based on the orthogonal test matrix analysis method, BP neural network algorithm, and genetic algorithm is proposed to carry out a multi-objective synergetic optimization algorithm study of the TFN, determine the order of influence of each parameter on the characteristic index, and obtain the optimal parameters under a multi-objective case [30]. First, a multi-objective synergetic optimization algorithm database is established by the orthogonal test method. Then, a balanced, intelligent, fast, and accurate optimization scheme is built using the complementary advantages and disadvantages of the orthogonal test matrix analysis method, BP neural network [31–33] and genetic algorithm [34] for calculating the optimal values within the interval of the operating parameters and parameters of the TFN. Finally, the values of each characteristic index are predicted. A flowchart of the multi-objective synergetic optimization algorithm scheme is shown in Figure 12.

4.2 Establishment of Multi-Objective Synergetic Optimization Database

According to previous research results [35] and engineering application requirements, six key optimization parameters were selected: Gas flow Q_1, water flow Q_2, orifice diameter D, orifice depth L, distance between the SVC and the outlet of nozzle S, and the nozzle outlet diameter H. The droplet size d_s, effective atomization range b_s and sound pressure level (SPL) a_s of the TFN were considered as the main characteristic indicators. An orthogonal test scheme with six factors and five levels was adopted to establish an initial database for the BP

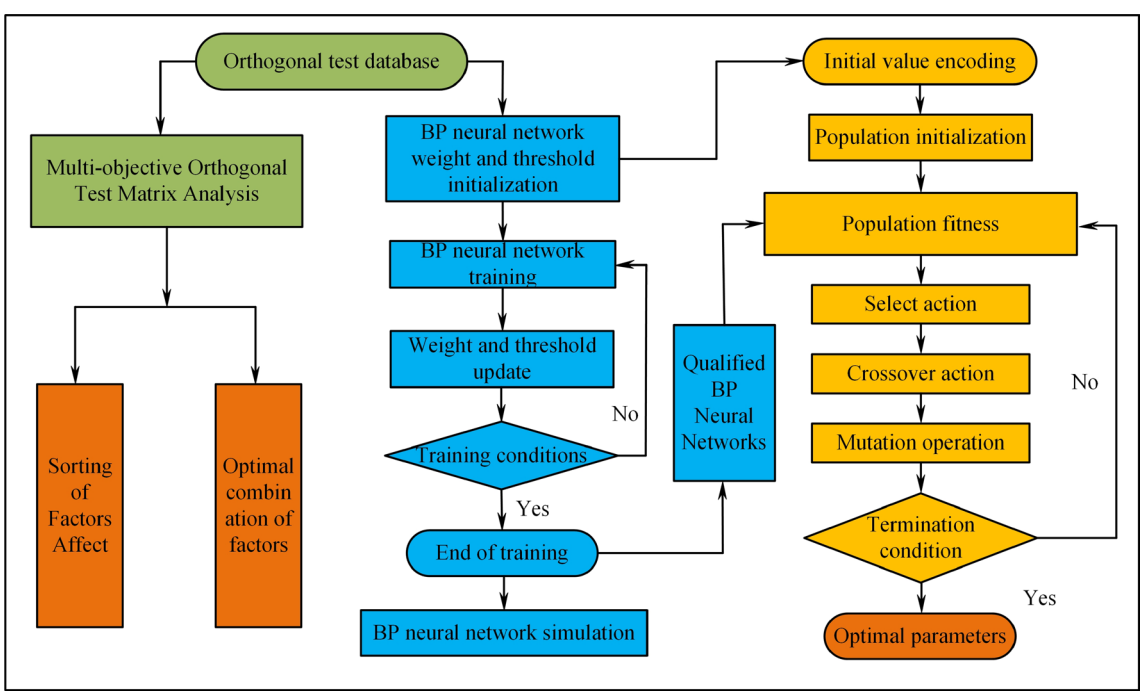

Figure 12 Flow chart of multi-objective synergetic optimization scheme

Table 6 Initial values and ranges

Optimization parameters	Initial value	Ranges
A Gas flow Q_1 (m^3/h)	1.0	0.8–1.2
B Water flow Q_2 (m^3/h)	0.035	0.025–0.045
C Orifice diameter *D* (mm)	2.0	1.0–3.0
D Orifice depth *L* (mm)	1.5	0.5–2.5
E Distance *S* (mm)	4.0	2.0–6.0
F Nozzle outlet diameter *H* (mm)	2.3	1.3–3.3

neural network. The ranges of the values for the six key optimization parameters are listed in Table 6.

According to the initial values and value ranges of the six key optimization parameters shown in Table 6, a multi-objective and multi-parameter $L_{25}(5^6)$ orthogonal test plan was formulated. A point 400 mm away from the TFN exit center point was used as a reference, and the results of the combination of different parameters and the multi-physics coupled acoustic-mechanics numerical simulation are shown in Table 7.

4.3 Establishment of BP Neural Network

The data obtained using the $L_{25}(5^6)$ orthogonal test scheme were used as the initial training database for the BP neural network. Through repeated training, the network learns the nonlinear laws hidden in the data. The qualified BP neural network has a high degree of nonlinear global effects, strong self-adaptive self-learning ability, and a high degree of parallelism.

5 Results and Discussion

5.1 Multi-Objective Orthogonal Test Matrix Analysis

Taking the droplet size (d_s), effective atomization range (b_s), and sound pressure level (SPL) (a_s) of the twin-fluid nozzle (TFN) as the main evaluation indicators, the multi-objective synergetic orthogonal simulation method shown in Table 7 was utilized using the

Table 7 $L_{25}(5^6)$ orthogonal test scheme and results

No.	Test factor						Particle size d_s (μm)	Range b_s (m)	SPL a_s (dB)
	A Gas flow Q_1 (m^3/h)	B Water flow Q_2 (m^3/h)	C Orifice diameter *D* (mm)	D Orifice depth *L* (mm)	E Distance *S* (mm)	F Nozzle outlet diameter *H* (mm)			
1	0.8	0.025	1.0	0.5	2.0	1.3	46.18	2.53	61.14
2	0.8	0.030	1.5	1.0	3.0	1.8	48.06	1.68	59.68
3	0.8	0.035	2.0	1.5	4.0	2.3	44.91	2.07	77.53
4	0.8	0.040	2.5	2.0	5.0	2.8	58.17	1.33	74.55
5	0.8	0.045	3.0	2.5	6.0	3.3	33.38	1.75	73.09
6	0.9	0.025	1.5	1.5	5.0	3.3	37.06	1.80	50.59
7	0.9	0.030	2.0	2.0	6.0	1.3	33.99	3.24	63.06
8	0.9	0.035	2.5	2.5	2.0	1.8	61.93	2.48	58.39
9	0.9	0.040	3.0	0.5	3.0	2.3	73.27	2.55	80.42
10	0.9	0.045	1.0	1.0	4.0	2.8	42.18	1.92	66.34
11	1.0	0.025	2.0	2.5	3.0	2.8	44.92	2.82	59.76
12	1.0	0.030	2.5	0.5	4.0	3.3	40.79	2.35	52.98
13	1.0	0.035	3.0	1.0	5.0	1.3	70.72	2.14	60.10
14	1.0	0.040	1.0	1.5	6.0	1.8	32.85	2.02	53.82
15	1.0	0.045	1.5	2.0	2.0	2.3	51.04	2.61	79.32
16	1.1	0.025	2.5	1.0	6.0	2.3	37.72	3.02	58.79
17	1.1	0.030	3.0	1.5	2.0	2.8	74.90	1.67	66.64
18	1.1	0.035	1.0	2.0	3.0	3.3	37.04	2.86	61.47
19	1.1	0.040	1.5	2.5	4.0	1.3	72.42	2.04	75.46
20	1.1	0.045	2.0	0.5	5.0	2.3	61.45	3.43	62.36
21	1.2	0.025	3.0	2.0	4.0	1.8	34.09	1.59	80.74
22	1.2	0.030	1.0	2.5	5.0	2.3	37.35	1.31	59.32
23	1.2	0.035	1.5	0.5	6.0	2.8	31.58	2.63	70.26
24	1.2	0.040	2.0	1.0	2.0	3.3	66.40	2.12	51.84
25	1.2	0.045	2.5	1.5	3.0	1.3	56.45	1.72	75.33

Table 8 Matrix analysis model

Hierarchical structure	Model
Target layer	Droplet size, Effective range of atomization, SPL
Factor layer	A; B; C; D; E; F
Horizontal layer	A_1–A_5; B_1–B_5; C_1–C_5; D_1–D_5; E_1–E_5; F_1–F_5

multi-physics coupled method. A test scheme (columns 2–7 in Table 7) was adopted, and the results of each evaluation index were calculated and obtained (columns 8–10 in Table 7).

To obtain the main factors of the characteristic index of the TFN under multiple objectives and the order of influence of each parameter, an orthogonal test matrix analysis was adopted to calculate the weights of each factor and each level of influence on the characteristic index; the optimal experimental scheme and order of effect of each parameter were determined according to the magnitude of the weight values.

Based on the results obtained in Table 7 for the multi-objective orthogonal test plan, a multi-objective orthogonal test matrix analysis model was established, as shown in Table 8.

According to the data in Table 7, the target layer, factor layer, and horizontal layer matrix of each characteristic index in the multi-objective case were established. k_{ij} was defined as the arithmetic mean of the results obtained at the jth level of factor i. At the same time, it was considered that the smaller the target expectation of the droplet size and SPL, the better, while the larger the target expectation of the effective atomization range. If the target layer matrix is $\boldsymbol{M}$, $\boldsymbol{M_d}$ is the target layer matrix of the droplet size, $\boldsymbol{M_b}$ is the target layer matrix of the effective range of atomization, and $\boldsymbol{M_a}$ is the target layer matrix of the SPL.

In some target orthogonal test schemes, the larger was the expected value of the target, the better (such as the effective range of atomization). The target layer matrix is expressed as:

$$\boldsymbol{M} = \begin{bmatrix} k_{11} & 0 & 0 & \cdots & 0 \\ \cdots & \cdots & \cdots & \cdots & \cdots \\ k_{15} & 0 & 0 & \cdots & 0 \\ 0 & k_{21} & 0 & \cdots & 0 \\ \cdots & \cdots & \cdots & \cdots & \cdots \\ 0 & k_{25} & 0 & \cdots & 0 \\ \cdots & \cdots & \cdots & \cdots & \cdots \\ 0 & 0 & 0 & \cdots & k_{61} \\ \cdots & \cdots & \cdots & \cdots & \cdots \\ 0 & 0 & 0 & \cdots & k_{65} \end{bmatrix}. \tag{8}$$

In some target orthogonal test schemes, the smaller the expected value of the target was, the better (such as the droplet size and SPL). The matrix of the target layer is expressed as:

$$\boldsymbol{M} = \begin{bmatrix} k_{11}^{-1} & 0 & 0 & \cdots & 0 \\ \cdots & \cdots & \cdots & \cdots & \cdots \\ k_{15}^{-1} & 0 & 0 & \cdots & 0 \\ 0 & k_{21}^{-1} & 0 & \cdots & 0 \\ \cdots & \cdots & \cdots & \cdots & \cdots \\ 0 & k_{25}^{-1} & 0 & \cdots & 0 \\ \cdots & \cdots & \cdots & \cdots & \cdots \\ 0 & 0 & 0 & \cdots & k_{61}^{-1} \\ \cdots & \cdots & \cdots & \cdots & \cdots \\ 0 & 0 & 0 & \cdots & k_{65}^{-1} \end{bmatrix}. \tag{9}$$

$T_i = 1 \Big/ \sum_{j=1}^{5} k_{ij}$, where $\sum_{j=1}^{5} k_{ij}$ denotes the sum of the arithmetic mean values of the results obtained at each level of factor i, defines the factor layer matrix as $\boldsymbol{T}$, where $\boldsymbol{T_d}$ is the factor layer matrix of the droplet particle size, $\boldsymbol{T_b}$ is the factor layer matrix of the effective range of atomization, and $\boldsymbol{T_a}$ is the factor layer matrix of the SPL. The specific description of the factor layer matrix is as follows:

$$\boldsymbol{T} = \begin{bmatrix} T_1 & 0 & \cdots & 0 \\ 0 & T_2 & \cdots & 0 \\ \cdots & \cdots & \cdots & \cdots \\ 0 & 0 & \cdots & T_6 \end{bmatrix}. \tag{10}$$

$S_i = R_i \Big/ \sum_{i=1}^{6} R_i$, where R_i denotes the range of the ith factor in the orthogonal test, then the horizontal layer matrix is defined as $\boldsymbol{S}$, where $\boldsymbol{S_d}$ is the horizontal layer matrix of the droplet particle size, $\boldsymbol{S_b}$ is the horizontal layer matrix of the effective range of atomization, and $\boldsymbol{S_a}$ is A matrix of the horizontal layers for SPL. The horizontal layer matrix is described in detail as follows:

$$\boldsymbol{S} = \begin{bmatrix} S_1 & S_2 & \cdots & S_6 \end{bmatrix}^{\mathrm{T}}. \tag{11}$$

Determining the weight of each target is key in the multi-objective orthogonal experiment matrix analysis, as it affects the precision of the results for each factor in the global optimization. The total weight matrix of the target value is expressed as:

$$\boldsymbol{\omega} = \boldsymbol{MTS} = [\omega_{A1}, \omega_{A2}, \omega_{A3}, \omega_{A4}, \omega_{A5}, \cdots, \omega_{F1}, \omega_{F2}, \omega_{F3}, \omega_{F4}, \omega_{F5}]^{\mathrm{T}}. \tag{12}$$

$\omega_{Aj} = K_{1j} T_1 S_1$ represents the weight value of the effect of the jth level of factor A on the target. This can reflect the degree of impact of this level on the target and can serve as the range of factor A.

If $\boldsymbol{\omega_d}$ is the weight matrix of the droplet size, $\boldsymbol{\omega_b}$ is the weight matrix of the effective range of atomization, and $\boldsymbol{\omega_a}$ is the weight matrix of the SPL, the calculation

Table 9 Total weight matrix value of multi-objective evaluation

Weight matrix	Numerical value	Weight matrix	Numerical value	Weight matrix	Numerical value
ω_{A1}	0.026560	ω_{C1}	0.041276	ω_{E1}	0.033101
ω_{A2}	0.029612	ω_{C2}	0.037325	ω_{E2}	0.034881
ω_{A3}	0.030167	ω_{C3}	0.041130	ω_{E3}	0.034803
ω_{A4}	0.029678	ω_{C4}	0.037350	ω_{E4}	0.034137
ω_{A5}	0.026943	ω_{C5}	0.033206	ω_{E5}	0.044744
ω_{B1}	0.036257	ω_{D1}	0.036967	ω_{F1}	0.029326
ω_{B2}	0.033151	ω_{D2}	0.034617	ω_{F2}	0.030344
ω_{B3}	0.032796	ω_{D3}	0.031827	ω_{F3}	0.030336
ω_{B4}	0.028589	ω_{D4}	0.034595	ω_{F4}	0.028956
ω_{B5}	0.031490	ω_{D5}	0.033091	ω_{F5}	0.032748

Table 10 Results of multi-objective orthogonal test matrix analysis

Category	Results					
Sensitivity of each factor	A	B	C	D	E	F
Percentage (%)	14.3	16.2	19.0	17.1	18.2	15.2
Factors affecting the order of priority	C>E>D>B>F>A					
The optimal level of each factor	A_3; B_1; C_1; D_1; E_5; F_5					
Optimal factor level combination	$A_3B_1C_1D_1E_5F_5$					

formula of the total weight matrix $\boldsymbol{\omega_T}$ of the multi-objective is:

$$\boldsymbol{\omega_d = M_d T_d S_d,\ \omega_b = M_b T_b S_b,\ \omega_a = M_a T_a S_a,} \tag{13}$$

$$\boldsymbol{\omega_T = (\omega_d + \omega_b + \omega_a)/3.} \tag{14}$$

According to the data in Table 7 and in combination with Eqs. (8)–(14), the total weight matrix value of the multi-objective evaluation was calculated and is shown in Table 9. Based on the calculation of the total weight matrix value of the multi-objective evaluation presented in Table 9, the weight value of each different factor and the optimal level of each factor can be obtained. By comparing the weight values of different factors, the primary and secondary order of the effect of various factors on the multi-objective evaluation, and the optimal combination of the factor levels can be obtained.

It can be seen from the total weight matrix value of the multi-objective evaluation in Table 9 that the maximum values of the comprehensive total weight of the five levels of each factor for the droplet size, effective range of atomization, and SPL are A_3=0.030167, B_1=0.036257, C_1=0.041276, D_1=0.036967, E_5=0.044744, and F_5=0.032748, respectively. It can be seen that from among the six optimization parameters selected in this study, compared with the other parameters, the parameters of the SVC have an evident influence on the multi-characteristic indices, and that the influence of the diameter D of the SVC is dominant.

Based on the orthogonal test matrix analysis, the optimal combination of factors was determined as $A_3B_1C_1D_1E_5F_5$ in the multi-objective case. The optimal result of the comprehensive analysis is: A gas flow rate of 1.0 m^3/h, water flow rate of 0.025 m^3/h, orifice diameter of 1.0 mm, orifice depth of 0.5 mm, distance between SVC and the outlet of nozzle of 6.0 mm, and a nozzle outlet diameter of 3.3 mm. Table 10 presents the results of the matrix analysis.

5.2 BP Neural Network Multi-Objective Prediction

To further increase the stability and convergence training speed of the BP neural network, the initial training database of the $L_{25}(5^6)$ orthogonal test scheme, as shown in Table 7, was expanded.

In the interval set by each optimization parameter, the original gas flows of 0.8, 0.9, 1.0, 1.1, 1.2 were replaced with 0.85, 0.95, 1.05, 1.15, and 1.17, respectively, and the numerical simulation calculation was carried out and 25 new groups of samples were obtained. Then, the water

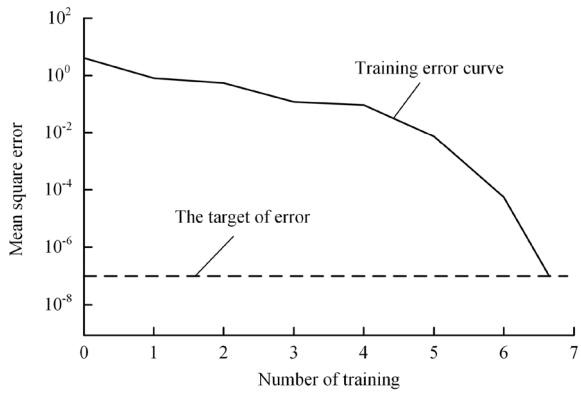

Figure 13 Training process error curve of BP neural network

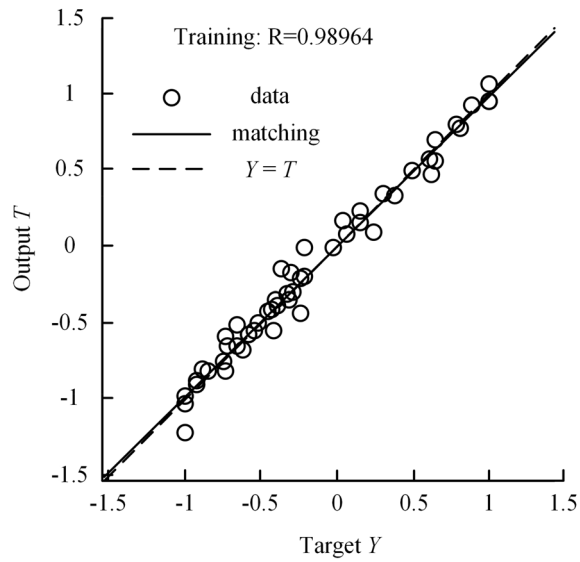

Figure 14 Matching result of sample data for BP neural network

flows of 25, 30, 35, 40, and 45 were replaced with 27.5, 32.5, 37.5, 41.5, and 43.5, respectively, and the numerical simulation calculation was carried out and 25 new groups of samples were obtained. From this, a total of 75 sets of samples were obtained as BP neural network sample training database.

The BP neural network established in Section 4.3 was used and was trained using the 75 sets of sample data mentioned above. Figure 13 shows the error curve of the BP neural network training process.

As shown in Figure 13, the mean square error at the beginning of training was relatively large. With the forward feedback on the error during the training process, the weights and thresholds were continuously updated. Simultaneously, the training error gradually decreased and approached the target error (1×10^{-7}) step-by-step. With an increase in the training time, the approximation speed of the training error was greatly improved, indicating that the nonlinear mapping ability of the input and output of this BP neural network was greatly improved after training and learning. The BP neural network requires only seven training cycles to achieve the set high convergence accuracy, which shows that the BP neural network structure established in Section 4.3 is reliable, and that the parameter settings are reasonable.

The sample data-matching results of the BP neural network obtained after seven feedback trainings are shown in Figure 14, whereby the fitting degree between the simulated output of the BP neural network and the actual output was as high as 98.96%. This indicates that the BP neural network has a good fitting effect, and that its nonlinear mapping ability between the input and output is very strong. This matching result further demonstrates the correctness of the BP neural network structure established in Section 4.3 and the rationality of the parameter setting.

5.3 Optimal Parameters for Multi-Objective Synergetic Optimization Algorithm

To achieve seamless parameter optimization within the interval, the value range of each key optimization parameter in Table 6 was used as the parameter optimization interval of the genetic algorithm, and the mature BP neural network (trained as described in Section 4.3) was applied to compute the individual adaptation of the population in the genetic algorithm. Finally, the optimum solution for the parameter was determined by searching in parallel within the global scope of the parameter search interval.

Based on the co-optimization method of the BP neural network and GA, the genetic algorithm program compiled using the mathematical software MATLAB was used for the calculation. When the operation reached 500 generations, the program ended. Figure 15 shows the optimization process of the GA evolution.

As shown in Figure 15(a), the droplet size gradually approached the optimal solution with the evolution of the GA. This phenomenon is mainly due to the selection, crossover, and mutation operations of the GA. Under the biological evolutionary group optimization mechanism of "survival of the fittest," excellent genes are retained and continue to evolve, the droplet size gradually decreases and eventually becomes stable, and the target value gradually approaches the global optimal solution of 18.18 μm. The effective fogging range in Figure 15(b) increases stepwise as the number of the evolutionary generations increases, and the value of the effective fogging range basically tends to a stable state after 300 generations of evolution, indicating that the effective fogging range has

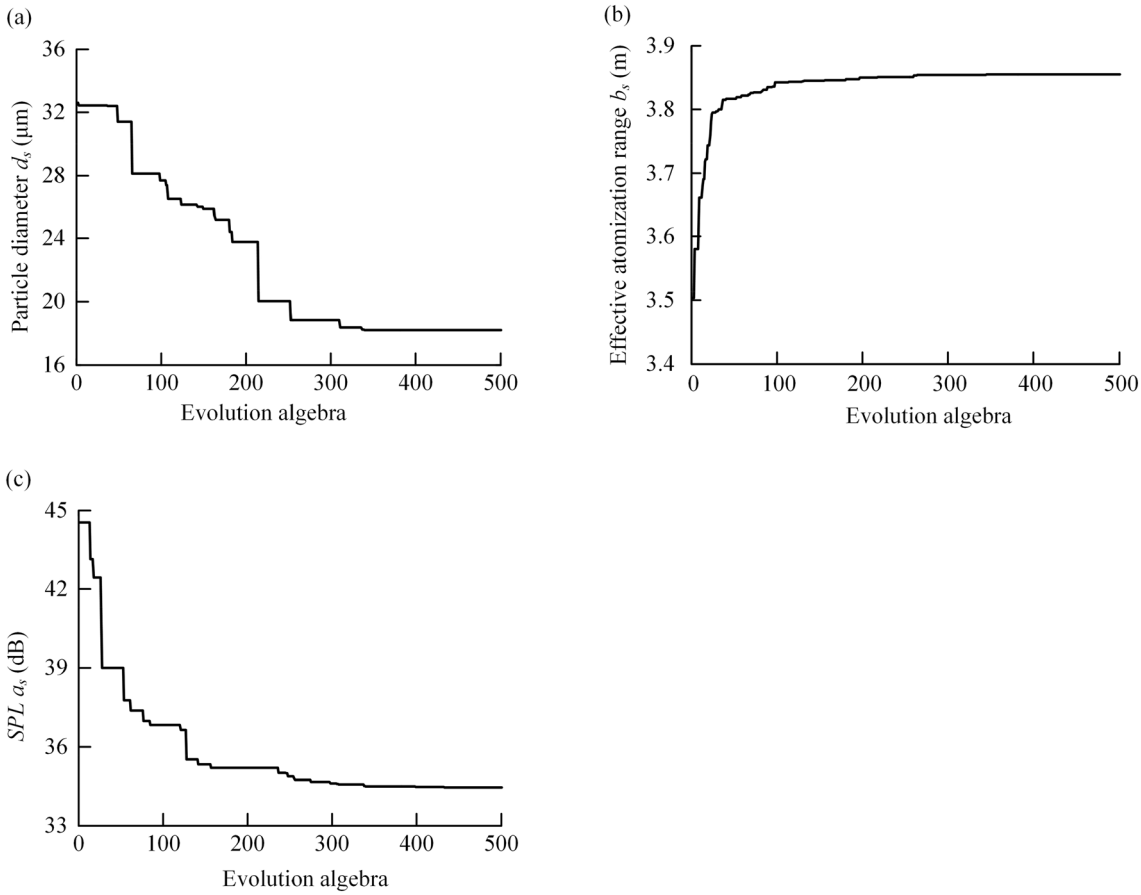

Figure 15 Optimization process of GA evolution: (**a**) Droplet size, (**b**) Effective range of atomization, (**c**) SPL

reached the global optimal solution of 3.86 m at this time. The SPL in Figure 15(c) decreases step-by-step as the evolutionary generations increase; when the number of generations reaches 400, the process of finding the optimal target value for the SPL ends, and the global optimal solution of the SPL is 34.45 dB.

After the global optimization of the GA was completed, the physics optimization algorithm process was completed, and the global optimal parameter value and optimal target result were obtained through a multi-objective synergetic optimization algorithm. Table 11 presents the comparative results before and after the multi-objective synergetic optimization algorithm.

As shown in Table 11, after multi-objective synergetic optimization, the orifice diameter and orifice depth of the TFN have significantly changed, the effective range of atomization has been significantly improved, the droplet size has been greatly improved, the SPL has dropped significantly, and the three objectives have been well optimized in the expected direction.

5.4 Comparative Analysis of Multi-Objective Synergetic Optimization Results

To further verify that the optimal parameters and optimal target results were obtained, a new physical model using optimal parameters is required, and a multi-physics coupled acoustic-mechanics numerical simulation of the TFN is performed. The specific parameters of each TFN are listed in Table 12, where nozzle No. 3 is the TFN before optimization and nozzle No. 5 is the TFN after optimization. To intuitively recognize the effects of the water flow on the noise and SMD of the droplets, nozzles 1, 2, and 4 shown in Table 12 were established.

Table 11 Comparison of results of multi-variable multi-objective optimization

Category	Optimization parameters					
	Gas flow Q_1 (m^3/h)	Water flow Q_2 (m^3/h)	Orifice diameter D (mm)	Orifice depth L (mm)	Distance S (mm)	Nozzle outlet diameter H (mm)
Before optimization	1.0	0.035	2.0	1.5	4.0	2.3
After optimization	0.94	0.0273	1.19	0.53	5.11	3.15
Rate of change (%)	6.00	22.00	40.50	64.67	27.75	36.96

Category	Target result		
	Droplet size d_s (μm)	Effective range of atomization b_s (m)	SPL a_s (dB)
Before optimization	34.82	2.25	63.82
After optimization	18.18	3.86	34.45
Rate of change (%)	47.79	71.56	46.02

Table 12 Detailed parameters of each TFN

Nozzle number	Nozzle parameters					
	Gas flow Q_1 (m^3/h)	Water flow Q_2 (m^3/h)	Orifice diameter D (mm)	Orifice depth L (mm)	Distance S (mm)	Nozzle outlet diameter H (mm)
No. 1	1.0	0.025	2.0	1.5	4.0	2.3
No. 2	1.0	0.030	2.0	1.5	4.0	2.3
No. 3	1.0	0.035	2.0	1.5	4.0	2.3
No. 4	1.0	0.040	2.0	1.5	4.0	2.3
No. 5	0.94	0.0273	1.19	0.53	5.11	3.15

Figure 16 shows the droplet SMD values at different positions on the central axis of the TFN. The optimization effect of the droplet SMD on different measuring points in space was remarkable. The multi-objective synergetic optimization algorithm achieved the goal of reducing the droplet size.

Figure 17 shows the SPL curves of the TFN before and after optimization. Within the range of the data collected, the maximum SPL value of the optimized No. 5 nozzle was smaller than that of the minimum value of the No. 3 nozzle, the minimum drop in the data of each corresponding measurement point was 25.74%, and the maximum was 52.11%. The multi-objective synergetic optimization algorithm was more effective, and the SPL performance in the atomized flow field was significantly improved.

The effective range of atomization reflects the spatial dispersion ability of the droplets. To visually analyze and compare the change in the effective range of atomization before and after the optimization of the TFN, a multi-physics coupled acoustic-mechanics numerical simulation method was applied in the calculation of the atomization space flow field of No. 3 nozzle before optimization and No. 5 nozzle after optimization.

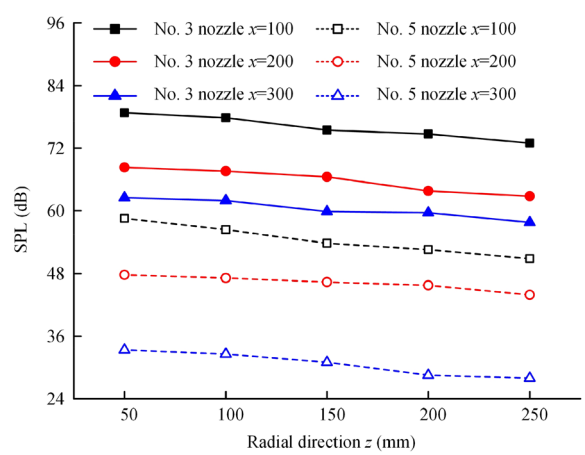

Figure 16 Comparison of SMD curves of different TFN

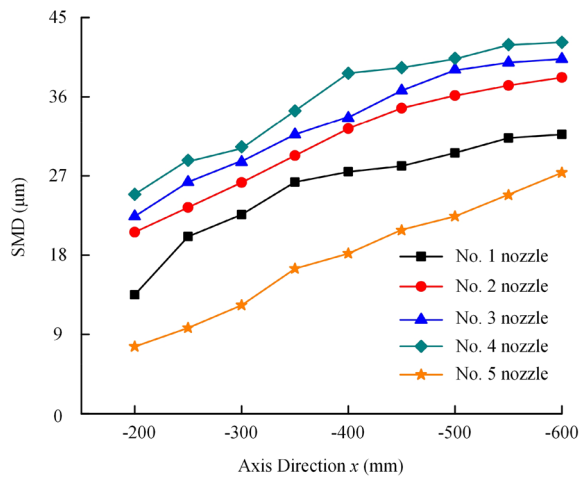

Figure 17 Comparison of SPL curves of nozzles before and after optimization

Figure 18 shows a comparison of the effective range of atomization before and after optimization of the TFN. It is evident that the axial distance of nozzle No. 5 in the atomization flow field space significantly increased by 71.56% compared with that of No. 3 nozzle before optimization. Moreover, although the optimized operating parameters were reduced compared with those before optimization, the motion ability of the droplet did not weaken, which indicates that the changes in the SVC parameters influence the energy carried by the droplets and their spatial motion behavior. After optimization, the properties (droplet size, spray range, and SPL) of the TFN improved, which was beneficial for improving the atomization behavior for wet dust removal.

6 Conclusions

In this study, a method combining a multi-physics coupled acoustic-mechanics numerical simulation and an intelligent synergetic optimization algorithm was adopted for optimizing the key parts of the overall structure of the TFN. The main conclusions are as follows.

(1) Based on the analysis results of the multi-physics coupled acoustic-mechanics numerical simulation, the effect of the water flow on the characteristics of

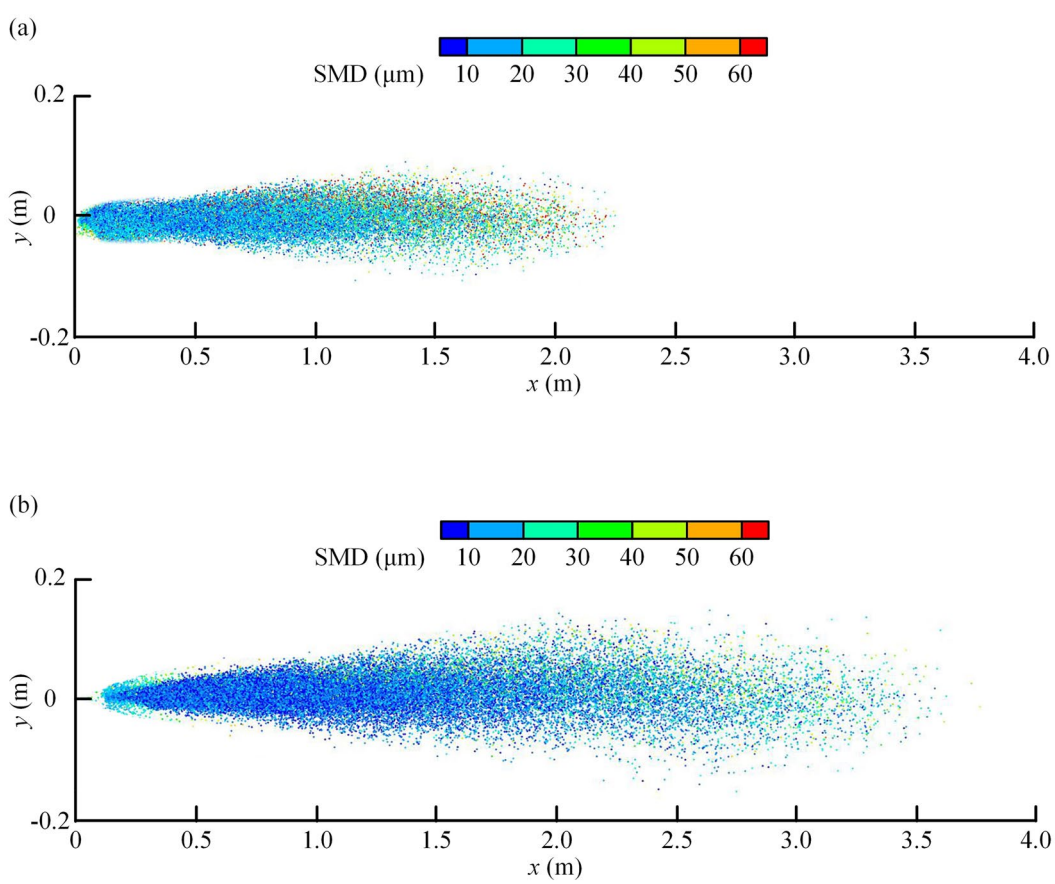

Figure 18 Comparison of atomizing range of TFN before and after optimization: (**a**) Before optimization, (**b**) After optimization

the atomization flow field was obtained. As the water flow increases, the velocity of the external flow field of the TFN first increases and then becomes stable, while the SPL of the TFN in the axial direction decreases first and then increases. At a water flow rate of 0.035 m^3/h, the SPL reached a minimum value of approximately 9.8% of the maximum value.

(2) The orthogonal test matrix analysis method was applied to perform parameter optimization analysis for the TFN, and the optimal combination of factors was obtained in the case of multiple objectives. The optimal result of the comprehensive analysis is: a gas flow rate of 1.0 m^3/h, water flow rate of 0.025 m^3/h, SVC orifice depth of 0.5 mm, SVC orifice diameter of 1.0 mm, distance between SVC and the outlet of TFN of 6.0 mm, and nozzle outlet diameter of 3.3 mm.

(3) The multi-objective synergetic optimization algorithm method is applied to synergistically optimize the parameters of TFN, and the optimal combination of parameters is obtained: a gas flow rate of 0.94 m^3/h, water flow rate of 0.0237 m^3/h, and SVC orifice diameter of 1.19 mm, SVC orifice depth of 0.53 mm, distance between SVC and the outlet of TFN of 5.11 mm, and nozzle outlet diameter of 3.15 mm.

(4) In the distance enhancement predicted by the multi-objective synergetic optimization algorithm method, the optimized droplet particle size in the atomization flow field space was significantly reduced, and the spray distance enhancement reached 71.56%. The reduction in the sound pressure level (SPL) data at each corresponding measurement point was 25.74% at the minimum and 52.11% at the maximum.

Acknowledgements
Not applicable.

Authors' Contributions
LZ and YBL were in charge of the entire trial; WL and YYL wrote the manuscript; YJL and JX assisted with the laboratory analyses; and BC assisted with the model. All authors read and approved the final manuscript.

Funding
Supported by National Natural Science Foundation of China (Grant No. U21A20122), Zhejiang Provincial Natural Science Foundation of China (Grant No. LY22E050012), China Postdoctoral Science Foundation (Grant Nos. 2023T160580, 2023M743102), Open Foundation of the State Key Laboratory of Fluid Power and Mechatronic Systems of China (Grant No. GZKF-202225), Students in Zhejiang Province Science and Technology Innovation Plan of China (Grant No. 2023R403073).

Data availability
The data that support the findings of this study are available on request from the author, Zhang Li, upon reasonable request.

Declarations

Competing Interests
The authors declare no competing financial interests.

Received: 5 September 2023 Revised: 15 April 2024 Accepted: 25 April 2024
Published online: 22 May 2024

References

[1] H Fan, C F Zhao, Y K Yang. A comprehensive analysis of the spatio-temporal variation of urban air pollution in China during 2014–2018. *Atmospheric Environment*, 2020, 220: 117066.
[2] R Akhbarizadeh, S Dobaradaran, M A Torkmahalleh, et al. Suspended fine particulate matter (PM2.5), microplastics (MPs), and polycyclic aromatic hydrocarbons (PAHs) in air: Their possible relationships and health implications. *Environmental Research*, 2021, 192: 110339.
[3] F H Zhang, H F Liu, J C Xu, et al. Experimental investigation on noise of cavitation nozzle and its chaotic behaviour. *Chinese Journal of Mechanical Engineering*, 2013, 26: 758-762.
[4] A Chowdhury, H G Johnston, C V Mashuga, et al. Effect of particle size and polydispersity on dust entrainment behind a moving shock wave. *Experimental Thermal and Fluid Science*, 2018, 93: 1-10.
[5] S K Chaulya, A Chowdhury, S Kumar, et al. Fugitive dust emission control study for a developed smart dry fog system. *Journal of Environmental Management*, 2021, 285: 112116.
[6] V Kosyanchuk, A Yakunchikov. Separation of a binary gas mixture outflowing into vacuum through a micronozzle. *Physics of Fluids*, 2021, 33(8): 082007.
[7] N Saleki-Haselghoubi, M T Shervani-Taba, M Taeibi-Rahni, et al. Numerical study on the oscillation of a transient bubble near a confined free surface for droplet generation. *Theoretical and Computational Fluid Dynamics*, 2014, 28: 449-472.
[8] Y Y Zhang, R F Hu, X J Zheng. Large-scale coherent structures of suspended dust concentration in the neutral atmospheric surface layer: A large-eddy simulation study. *Physics of Fluids*, 2018, 30(4): 046601.
[9] L Zheng, R Zhao, Y L Nian, et al. Numerical and experimental study of the effects of tangential to axial velocity ratio and structural parameters inside the nozzle on spray characteristics. *Physics of Fluids*, 2023, 35(4).
[10] X Y Zhou, Z L Hu, Y J Tao, et al. Failure mechanisms and structural optimization of shredder hammer for metal scraps. *Chinese Journal of Mechanical Engineering*, 2016, 29(4): 792-801.
[11] Q Q Zhou, X Y Xue, W C Qin, et al. Optimization and test for structural parameters of UAV spraying rotary cup atomizer. *International Journal of Agricultural and Biological Engineering*, 2017, 10(3): 78-86.
[12] Z X Li, T D Manh, M B Gerdroodbary, et al. The effect of sinusoidal wall on hydrogen jet mixing rate considering supersonic flow. *Energy*, 2020, 193: 116801.
[13] P F Wang, H Han, R H Liu, et al. Effect of outlet diameter on atomization characteristics and dust reduction performance of X-swirl pressure nozzle. *Process Safety and Environmental Protection*, 2020, 137: 340-351.
[14] K M Akkoli, N R Banapurmath, M M Shivashimpi et al. Effect of injection parameters and producer gas derived from redgram stalk on the performance and emission characteristics of a diesel engine. *Alexandria Engineering Journal*, 2021, 60(3): 3133-3142.
[15] Y J Li, P F Wang, R H Liu, et al. Determination of the optimal axial-to-radial flow ratio of the wall-mounted swirling ventilation in fully mechanized excavation face. *Powder Technology*, 2020, 360: 890-910.
[16] J S Thompson, O Hassan, S A Rolland, et al. The identification of an accurate simulation approach to predict the effect of operational parameters on the particle size distribution (PSD) of powders produced by an industrial close-coupled gas atomiser. *Powder Technology*, 2016, 291: 75-85.

[17] W Chen, L F Zhang, Y D Wang, et al. Prediction on the three-dimensional spatial distribution of the number density of inclusions on the entire cross section of a steel continuous casting slab. *International Journal of Heat and Mass Transfer*, 2022, 190: 122789.
[18] H K Foroushan, H A Jakobsen. On the dynamics of fluid particle breakage induced by hydrodynamic instabilities: A review of modelling approaches. *Chemical Engineering Science*, 2020, 219: 115575.
[19] J Jedelsky, M Jicha. Spray characteristics and liquid distribution of multi-hole effervescent atomisers for industrial burners. *Applied Thermal Engineering*, 2016, 96: 286-296.
[20] C S Jeong, C Y Lee. Experimental investigation on spray characteristics of twin-fluid nozzle for water mist and its heptane pool fire extinguishing performance. *Process Safety and Environmental Protection*, 2021, 148: 724-736.
[21] M L Pezo, L Pezo, D Dragojlovic, et al. Experimental and computational study of the two-fluid nozzle spreading characteristics. *Chemical Engineering Research and Design*, 2021, 166: 18-28.
[22] C Zhang, A G Li, J N Guo, et al. Jet noise reduction of spherical tuyeres with serrated trailing edges. *Journal of Building Engineering*, 2021, 44: 103324.
[23] B Chen, D R Gao, Y B Li, et al. Influence of atomizing core on droplet dynamic behavior and machining characteristics under synergistically enhanced twin-fluid spray. *The International Journal of Advanced Manufacturing Technology*, 2020, 110(9): 2269-2282.
[24] B Chen, D R Gao, Y B Li, et al. Investigation of the droplet characteristics and size distribution during the collaborative atomization process of a twin-fluid nozzle. *The International Journal of Advanced Manufacturing Technology*, 2020, 107(3): 1625-1639.
[25] P Cai, W Nie, D W Chen, et al. Effect of air flowrate on pollutant dispersion pattern of coal dust particles at fully mechanized mining face based on numerical simulation. *Fuel*, 2019, 239: 623-635.
[26] A Wawrzak, K Wawrzak, A Boguslawski, et al. Global instability phenomenon as a physical mechanism controlling dynamics of a nitrogen-diluted hydrogen flame. *International Journal of Heat and Mass Transfer*, 2023, 213: 124260.
[27] C L Xing, G G Le, L Shen, et al. Numerical investigations on acoustic environment of multi-nozzle launch vehicle at lift-off. *Aerospace Science and Technology*, 2020, 106: 106140.
[28] B Chen, D R Gao, Y N Liang, et al. Experimental investigation of atomization and droplet turbulence characteristics of a twin-fluid nozzle with different self-excited vibrating cavity structures. *Experimental Thermal and Fluid Science*, 2018, 99: 525-536.
[29] B Chen, D R Gao, Y B Li, et al. Experimental analysis of spray behavior and lubrication performance under twin-fluid atomization. *Journal of Manufacturing Processes*, 2021, 61: 561-573.
[30] S F Ding, C Y Su, J Z Yu. An optimizing BP neural network algorithm based on genetic algorithm. *Artificial Intelligence Review*, 2011, 36: 153-162.
[31] M Cerezo, P J Coles. Higher order derivatives of quantum neural networks with barren plateaus. *Quantum Science and Technology*, 2021, 6(3): 035006.
[32] C Li, Y j Liu, H L Zhang. An improved coal and gas outburst prediction algorithm based on BP neural network. *International Journal of Control and Automation*, 2015, 8(6): 169-176.
[33] L Zhang, F L Wang, T Sun, et al. A constrained optimization method based on BP neural network. *Neural Computing and Applications*, 2018, 29: 413-421.
[34] W J Duan, X Q Wang, S Y Cheng, et al. A new scheme of PM2.5 and O_3 control strategies with the integration of SOM, GA and WRF-CAMx. *Journal of Environmental Sciences*, 2024, 138: 249-265.
[35] L F Yin, T Wang, B M Zheng. Analytical adaptive distributed multi-objective optimization algorithm for optimal power flow problems. *Energy*, 2021, 216: 119245.

Wenying Li is currently a PhD candidate at *College of Mechanical Engineering, Zhejiang University of Technology, China*. Her primary research interests include fluid transmission, controls, and AM.

Yanying Li is currently a master's candidate at *School of Materials Science and Engineering, Northwestern Polytechnical University, China*.

Yingjie Lu is currently a PhD candidate at *College of Mechanical Engineering, Zhejiang University of Technology, China*.

Jinhuan Xu is currently a master's candidate at *College of Mechanical Engineering, Zhejiang University of Technology, China*.

Bo Chen is an associate professor at *College of Mechanical Engineering, Zhejiang University of Technology, China*.

Li Zhang is currently a professor at *College of Mechanical Engineering, Zhejiang University of Technology, China*.

Yanbiao Li is currently a professor at *College of Mechanical Engineering, Zhejiang University of Technology, China*.